

1 **The basic effect of cloud radiative effects on tropical sea-surface**
2 **temperature variability**

3 Ying Li* and David W. J. Thompson

4 *Department of Atmospheric Science, Colorado State University, Fort Collins, Colorado, USA*

5 Dirk Olonscheck

6 *Max Planck Institute for Meteorology, Hamburg, Germany*

7 *Corresponding author address: Ying Li, Department of Atmospheric Science, Colorado State
8 University, 3915 W. Laporte Ave. Fort Collins, CO 80521
9 E-mail: Ying.Li@colostate.edu

ABSTRACT

Cloud radiative effects (CREs) are known to play a central role in governing the long-term mean distribution of sea-surface temperatures (SSTs). Very recent work suggests that CREs may also play a role in governing the *variability* of SSTs in the context of the El Niño/Southern Oscillation. Here, the authors exploit numerical simulations with varying representations of CREs to demonstrate that coupling between CREs and the atmospheric circulation has a much more general and widespread effect on tropical climate than that indicated in previous work.

The results reveal that coupling between CREs and the atmospheric circulation leads to robust increases in SST variability on timescales longer than a month *throughout* the tropical oceans. It is argued that the increases in tropical SST variance derive primarily from the coupling between SSTs and shortwave CREs: Coupling increases the memory in shortwave CREs on hourly and daily timescales, and thus reddens the spectrum of shortwave CREs and increases their variance on timescales spanning weeks to decades. Coupling between SSTs and CREs does not noticeably affect the variance of SSTs in the extratropics, where the effects from variability in CREs on the surface energy budget are much smaller than the effects from the turbulent heat fluxes. The results indicate the basic but critical role of CREs in climate variability throughout the tropics.

30 **1. Introduction**

31 An increasing body of literature suggests that cloud radiative effects (CREs) play a key role
32 in governing not only the *mean* atmospheric circulation and its response to global warming, but
33 also its *variability* across a range of spatial and temporal scales. The advent of various remotely-
34 sensed cloud products such as those derived from the CloudSAT /CALIPSO (Stephens et al. 2002)
35 satellites has provided unprecedented insight into the vertical structure of clouds in the long-term
36 mean (Zhang et al. 2007; Su et al. 2011; Su and Jiang 2013; Li et al. 2014b), and into the signatures
37 of large-scale climate variability in various cloud properties in both the extratropics (Li et al.
38 2014a; Wall and Hartmann 2015; Li and Thompson 2016) and tropics (Eguchi and Shiotani 2004;
39 Masunaga et al. 2008; Chen and Genio 2009; Tromer and Rossow 2010; Jiang et al. 2011; Riley
40 et al. 2011; Ma and Kuang 2011; Yuan and Houze 2013; Crueger and Stevens 2015). Numerical
41 experiments run with varying representations of CREs have revealed the central role of clouds in
42 simulations of the mean tropospheric and stratospheric circulations (Fermepin and Bony 2014; Li
43 et al. 2015, 2017; Harrop and Hartmann 2016; Watt-Meyer and Frierson 2017), in the simulated
44 atmospheric circulation response to climate change (Ceppi et al. 2012, 2014; Ceppi and Hartmann
45 2015; Voigt and Shaw 2015, 2016; Ceppi and Hartmann 2016; Flaschner et al. 2018; Li et al. 2019;
46 Voigt et al. 2019), and in the amplitude of climate variability in the context of the MJO (Lee et al.
47 2001; Crueger and Stevens 2015) and the spectrum of tropical waves (Zurovac-Jevtic et al. 2006;
48 Lin et al. 2007).

49 Two recent studies have argued that cloud radiative feedbacks also play an important role in
50 governing the amplitude and periodicity of the El Niño/Southern Oscillation (ENSO) (Rädel et al.
51 2016; Middlemas et al. 2019). The studies both exploit “locked-clouds” experiments, but they
52 were run on different numerical models and used slightly different experimental frameworks. In

53 both studies, the effects of CREs on the circulation are estimated by comparing output from 1)
54 a control simulation where CREs are coupled to the atmospheric circulation and 2) a “locked-
55 clouds” simulation where the cloud-related properties input into the model radiation code are
56 decoupled from the atmospheric circulation. In the case of Middlemas et al. (2019), the CREs
57 in the locked simulation were determined by repeating values of the CREs derived from a single
58 sample year from the control simulation. As such, the CREs prescribed in the locked run have a
59 similar diurnal and seasonal cycle to those found in the control run, but no interannual variability.
60 In the case of Rädel et al. (2016), the CREs in the locked simulation were determined by random-
61 izing the year assigned to each radiation call time step in the control output. The two studies yield
62 slightly different results: Rädel et al. (2016) found that ENSO variability is enhanced across all
63 timescales when CREs are coupled to the atmospheric circulation due to positive longwave cloud
64 radiative feedbacks, whereas Middlemas et al. (2019) found ENSO variability is only enhanced
65 on timescales shorter than 6 years, but reduced on timescales longer than that due to negative
66 shortwave cloud radiative feedbacks.

67 One possible reason for the different responses in the two simulations is differences in the model
68 treatment of shortwave and longwave feedbacks (Lloyd et al. 2011, 2012; Bellenger et al. 2014).
69 For example, as discussed in Middlemas et al. (2019), the ENSO response to changes in cloud
70 properties depends on the relative amplitudes in the CESM1.2 and MPI models of 1) the model
71 short and longwave cloud radiative feedbacks relative to 2) the other model feedbacks that are
72 essential for the simulated ENSO variability.

73 Another possible reason is differences in the locking methodologies, in particular the effects of
74 the locking methodologies on the auto-correlation of the prescribed cloud fields. The “locked-
75 cloud” fields in Middlemas et al. (2019) consist of annually-repeating values drawn a single year
76 from the control. The cloud fields in the control and locked simulations thus have roughly the

⁷⁷ same autocorrelation. In contrast, the locked-cloud fields in Rädel et al. (2016) are randomized
⁷⁸ such that they have no memory on timescales longer than two hours. Here we argue that remov-
⁷⁹ ing the autocorrelation of the prescribed cloud fields is important for identifying the effects of
⁸⁰ cloud-circulation coupling on the atmosphere, since the autocorrelation in the cloud fields in the
⁸¹ control (interactive) simulation derives in large part from the memory inherent in the large-scale
⁸² atmospheric circulation

⁸³ Our hypothesis is that cloud-circulation coupling imparts memory to CREs that would not exist
⁸⁴ in the absence of forcing by the large-scale flow. This memory acts to increase the persistence
⁸⁵ of shortwave radiative fluxes at the surface, and the more-persistent shortwave fluxes are then
⁸⁶ integrated by the SST field. It is suggested that the basic effect of coupling between clouds and
⁸⁷ the atmospheric circulation is thus to redden the spectrum of shortwave CREs, hence reducing
⁸⁸ their variance on daily and shorter timescales but increasing their variance on monthly and longer
⁸⁹ timescales. The increased variance of shortwave CREs on monthly timescales, in turn, leads
⁹⁰ to notable increases in the SST variance over the tropics, where surface temperature variability
⁹¹ is dominated by the shortwave radiative flux. Importantly, the coupling between CREs and the
⁹² atmospheric circulation enhances the month-to-month variability of SSTs by a factor of 2–3 not
⁹³ only in the tropical Pacific, but *throughout* the tropical oceans. The coupling has little effect
⁹⁴ on SST variance over the extratropics, where surface temperature variability is dominated by the
⁹⁵ turbulent heat fluxes.

⁹⁶ 2. Locked-clouds simulations

⁹⁷ As in Rädel et al. (2016) and Middlemas et al. (2019), the influence of CREs on the circulation
⁹⁸ are assessed by comparing output from 1) a control simulation where CREs are coupled to the

99 atmospheric circulation and 2) a “locked-clouds” simulation where the CREs are prescribed and
100 thus decoupled from the circulation.

101 The simulations were run on the latest version of the Max Planck Institute Earth System Model
102 at low resolution (MPI-ESM1.2-LR), and with preindustrial forcing (note that the experiments in
103 Rädel et al. (2016) were run on an earlier version of the model: the MPI-ESM1.0-LR). The model
104 has T63 (\sim 200 km) horizontal resolution and 47 vertical layers in the atmosphere component
105 (ECHAM6.3), and nominal 1.5° horizontal resolution and 40 vertical layers in the ocean com-
106 ponent (MPIOM 1.6.3). The MPI-ESM1.2-LR is the baseline version used in the sixth Coupled
107 Model Intercomparison Project (Eyring et al. 2016).

108 The locked simulations were performed in an analogous manner as described in Rädel et al.
109 (2016) and Olonscheck et al. (2019). That is:

110 1) Key cloud parameters - including cloud cover fraction and cloud liquid/ice water content at all
111 vertical levels - were saved from a 250-year long control simulation at every two-hour radiation
112 call (note that key cloud parameters are saved just the first 50 years in Rädel et al. (2016)).

113 2) The cloud parameters from the control run were scrambled by randomizing the year assigned
114 to each time step, but not the hour or day. As such, the randomized cloud parameters have the
115 same long-term mean diurnal and seasonal cycles, have no memory from one time step to the
116 next (e.g., output at 00Z01Jan is assigned a different year than output at 02Z01Jan, etc), and
117 are decoupled from the circulation. As discussed below, the lack of autocorrelation in the cloud
118 fields plays an important role in changing the low-frequency variance of the attendant CREs.

119 3) The scrambled cloud fields were then read into the radiation code of the locked-clouds simula-
120 tion at every two-hour radiation call. The cloud locking method is only applied to the radiative
121 transfer scheme; all other model components use internally simulated clouds.

122 The control and locked-clouds simulations are both 250-yrs in length, but the first 50 years
123 of both simulations are discarded to account for the warming adjustment in the locked-clouds
124 simulation as mentioned above.

125 Decoupling the cloud fields from the circulation leads to a weak warm bias in the locked-clouds
126 simulations relative to the control run. A similar global-mean warming or cooling climate drift is
127 found in other locked-clouds simulations, and is thought to arise from the small artificial radiative
128 forcing that arises from the loss of spatio-temporal structure in clouds (Schneider et al. 1999;
129 Langen et al. 2012; Mauritsen et al. 2013; Rädel et al. 2016; Middlemas et al. 2019; Olonscheck
130 et al. 2019). It is possible that the weak warm bias in the locked simulation could affect the
131 variance of temperature in the polar regions, since the variability in sea ice coverage depends
132 on sea-ice thickness. For this reason, results are only shown equatorward of 70°S/N (readers are
133 referred to Olonscheck et al. (2019) for a more detailed discussion on sea ice changes in analogous
134 locking simulations). However, we view it unlikely that the small bias in mean temperature in the
135 tropics will have a notable effect on the temperature variance there: The differences in mean
136 temperature between the control and locked simulation are roughly an order of magnitude smaller
137 than typical span in mean temperature between coldest and warmest historical simulations in the
138 CMIP5 archive (Mauritsen et al. 2012).

139 **3. The influence of cloud radiative effects on tropical SST variability**

140 We focus our analysis on a comparison of month-to-month variability in 1) the control simula-
141 tion, where clouds are coupled to the circulation (hereafter referred to as the “interactive” clouds
142 run) and 2) the “locked” clouds run, where clouds are decoupled from the circulation. The differ-
143 ences in climate variability between the interactive and locked clouds simulations derive entirely
144 from the role of coupling between CREs and the circulation.

145 Figure 1a shows the variance of monthly-mean SST anomalies in the interactive-clouds run.
146 The simulated SST variability is most pronounced in regions where 1) upwelling is important
147 (e.g., along the equator and near coastal regions) and 2) ocean heat transport and atmospheric
148 temperature advection are important (e.g., the western boundary current regions). Figure 1b shows
149 the same results for the locked-clouds run. At first glance, the patterns of SST variance in the
150 control interactive and locked clouds runs appear to differ only in the eastern tropical Pacific. But
151 closer inspection of the results reveals marked differences *throughout* the tropical oceans.

152 Figure 1c shows the ratios of the SST variances in the interactive and locked clouds simulations.
153 Values greater than one indicate regions where coupling between CREs and the circulation acts
154 to increase the variance in SSTs, and vice versa. Areas where the variance ratios are statistically
155 significant at the 95% significance level based on the F-statistic are stippled. The most prominent
156 ratios in Fig. 1c are found at tropical latitudes, where coupled CREs lead to increases in month-
157 to-month SST variance by a factor of 2–3 across the tropical Indian, Pacific and Atlantic oceans.

158 The differences in area-averaged SST variances between the interactive and locked clouds sim-
159 ulations are shown as a function of frequency in the power spectra in Fig. 2. The differences are
160 dramatic. The variances in the interactive simulation are substantially increased on inter-annual
161 and decadal timescales across the entire tropics. The increases in variance over the Niño 3.4 re-
162 gion (Fig. 2a) are consistent with the amplification of El Niño event and Niño 3.4 power spectrum
163 found in Rädel et al. (2016, cf. Fig. 2a) and in Middlemas et al. (2019, on timescales less than
164 ~6 years, cf. Fig. 4a). The increases in variance in the tropical Indian (Fig. 2c), tropical western
165 Pacific (Fig. 2d), tropical North and South Atlantic (Figs. 2e,f) oceans are most pronounced on
166 timescales longer than ~5 years.

167 As demonstrated in Appendix Fig. B1, the increases in tropical SST variance transcend the
168 linear response to SST variability in the central and eastern tropical Pacific. In fact, as argued in

¹⁶⁹ Section 4, the differences in monthly-mean SST variance shown in Figs. 1c and B1 arise not from
¹⁷⁰ the projection of CREs onto ENSO per se, but rather from a more basic effect of CREs on surface
¹⁷¹ temperature.

¹⁷² The tropics-wide increases in SST variance are associated with a range of differences in vari-
¹⁷³ ous other tropical fields. They are associated with increases in the variance of upper tropospheric
¹⁷⁴ temperatures throughout the tropics (Fig. 3a), consistent with the facts that tropical atmospheric
¹⁷⁵ temperatures are strongly modulated by the SST field and closely follow the moist adiabatic lapse
¹⁷⁶ rate. (The increases in atmospheric temperature variance may also be influenced by positive long-
¹⁷⁷ wave cloud radiative feedbacks in the interactive simulation; Rädel et al. 2016). The tropics-wide
¹⁷⁸ increases in SST variance are associated with increases in the variances of convective precipitation
¹⁷⁹ (Fig. 3b), particularly over the tropical Pacific where the SST variance ratios are largest. And they
¹⁸⁰ are associated with increases in the variances of the upper tropospheric geopotential height field
¹⁸¹ (Fig. 3c). The increases in the variance of upper tropospheric geopotential height project onto
¹⁸² the structure of the model equatorial planetary waves, as evidenced by the close correspondence
¹⁸³ between 1) the equatorial troughs and ridges in the climatological-mean geopotential height field
¹⁸⁴ (black contours in Fig. 3d) and 2) the variance ratios in the eddy geopotential height field (shading
¹⁸⁵ in Fig. 3d).

¹⁸⁶ **4. Interpretation**

¹⁸⁷ *a. Surface energy budget*

¹⁸⁸ Figures 1 and 2 reveal marked increases in SST variance throughout the tropics in simulations
¹⁸⁹ run with interactive CREs. In this section, we quantify the physical factors that drive the increases
¹⁹⁰ in SST variance by diagnosing the attendant changes in the surface energy budget.

191 The energy budget for the surface mixed layer of the ocean can be expressed in monthly-mean
 192 anomaly form as:

$$C_o \frac{\partial T'}{\partial t} = Q'_{SW} + Q'_{LW} + Q'_{LH} + Q'_{SH} + Q'_{EK} + Q'_{geo}, \quad (1)$$

193 where primes denote monthly-mean anomalies (departures from the long-term mean seasonal cy-
 194 cle); T' is the anomalous temperature of the mixed layer (assumed proportional to the anomalous
 195 SST); C_o is the effective heat capacity of the mixed layer ($C_o = C_p \rho h$, in which ρ and C_p are the
 196 density and specific heat capacity at constant pressure of the seawater, i.e., $3850 \text{ J kg}^{-1}\text{C}^{-1}$), h is
 197 the annual-mean mixed layer depth taken from the ocean model; and the Q' are the heatings due
 198 to anomalous surface shortwave radiative flux (Q'_{SW}), longwave radiative flux (Q'_{LW}), latent heat
 199 flux (Q'_{LH}), sensible heat flux (Q'_{SH}), advection by the Ekman flow (Q'_{EK}) and advection by the
 200 surface geostrophic flow (Q'_{geo}). Here $Q_{EK} = -C_o \vec{V}_{EK} \cdot \nabla T$ and $Q_{geo} = -C_o \vec{V}_{geo} \cdot \nabla T$, in which
 201 \vec{V}_{EK} is the Ekman flow induced by the wind stress (τ) and \vec{V}_{geo} is the geostrophic currents. We
 202 neglect vertical advection and entrainment for simplicity, even though these processes are clearly
 203 important along the coastal and equatorial upwelling zones.

204 Following Yu and Boer (2006), Eq. 1 can be manipulated to yield an expression for the temper-
 205 ature variance by a) taking the centered difference of Eq. 1, b) squaring the result, and c) taking
 206 the time-mean. As reviewed in Appendix A, the above operation yields the following expression
 207 for the temperature variance:

$$\sigma_T^2 = G \cdot \sigma_\Sigma^2 \cdot e \quad (2)$$

208 where

- 209 • σ_T^2 is the variance of the SST field.

- 210 • $\sigma_{\Sigma}^2 = \sigma_{SW}^2 + \sigma_{LW}^2 + \sigma_{LH}^2 + \sigma_{SH}^2 + \sigma_{EK}^2 + \sigma_{geo}^2$ is the sum of the variances of the surface heat
 211 fluxes and ocean heat transport. Larger variances in the flux and transport terms lead to larger
 212 variance in the SST field, and vice versa.

- 213 • e includes the sum of the covariances between the heat flux terms (e.g., $e = 1 + \frac{2\Sigma(\text{cov}(Q_i, Q_j))}{\sigma_{\Sigma}^2}$),
 214 where $\Sigma(\text{cov}(Q_i, Q_j)) = \text{cov}(Q'_{SW}, Q'_{LH}) + \text{cov}(Q'_{SW}, Q'_{SH}) + \text{cov}(Q'_{SW}, Q'_{EK}) + \dots$). e may be
 215 viewed as an “efficiency factor” that measures the extent to which the variances in the flux and
 216 transport terms operate independently in modifying the SST variance (Yu and Boer 2006).
- 217 • $G = \frac{2(\Delta t)^2}{C_o^2(1-r_2)}$ may be viewed as a “transfer factor” that accounts for the effects on the temper-
 218 ature variance of the sampling timescale (Δt), the persistence (related to lag-2 autocorrelation
 219 r_2), and the effective heat capacity (C_o) (Yu and Boer 2006).

220 The left and middle columns in Fig. 4 explore the contributions of the individual terms in σ_{Σ}^2 to
 221 the variances in monthly-mean SSTs in the interactive and locked simulations. The right column
 222 shows the percent contributions of the individual variances in the left column to the total variances
 223 in the interactive run. The primary features in the figure are the following:

- 224 1) The largest variances in the surface energy budget are found in association with the latent heat
 225 fluxes and are located over the subtropical and midlatitude oceans (panels g and h).
- 226 2) The variances in the ocean heat transport peak over regions where the climatological-mean
 227 SST gradients are largest (panels m and n) (Alexander 1992), and the variances in the sensible
 228 heat fluxes peak over the western sides of the Northern Hemisphere ocean basins (panels j and
 229 k), where there is commonly cold-advection in the atmosphere from the continents upstream
 230 (Davis 1976; Miller 1992; Alexander 1992; Cayan 1992; Marshall et al. 2001; Alexander et al.
 231 2002).

232 3) In the interactive simulation, the variances in the shortwave radiative fluxes have relatively
 233 similar amplitude throughout the globe (panel a). As evidenced in panel c and discussed further
 234 below, the shortwave radiative fluxes account for a comparatively large fraction of the total
 235 variance in the energy budget over the tropics since the latent heat fluxes variance are weakest
 236 there. The variances in the longwave radiative fluxes are relatively small and account for a
 237 small fraction of the surface flux variance everywhere (panels d and f).

238 4) By far the most pronounced differences between the interactive and locked simulations are
 239 found in the variances of the shortwave fluxes. The variances in monthly-mean shortwave
 240 heat fluxes are $\sim 200 \text{ W}^2 \text{ m}^{-4}$ throughout much of the globe when clouds are coupled to the
 241 circulation (panel a), but less than $\sim 20 \text{ W}^2 \text{ m}^{-4}$ in the locked simulation (panel b). As such
 242 the shortwave variance ratios ($\frac{\sigma_{SW \text{ interactive}}^2}{\sigma_{SW \text{ locked}}^2}$) are as large as ~ 10 throughout much of the globe.
 243 As discussed below, the reduced variance of the monthly-mean all-sky shortwave radiative flux
 244 in the locked simulation arises from the “whitening” of CREs when clouds are decoupled from
 245 the circulation. That is, decoupling clouds from the circulation increases their variance on
 246 sub-daily timescales, but decreases their variance on weekly and longer timescales.

247 From Eq. 2, it follows that the ratios of temperature variance between the interactive and locked
 248 run can be diagnosed as:

$$\frac{\sigma_T^2 \text{ interactive}}{\sigma_T^2 \text{ locked}} = \frac{\sigma_\Sigma^2 \text{ interactive}}{\sigma_\Sigma^2 \text{ locked}} \cdot \frac{e_{interactive}}{e_{locked}} \cdot \frac{G_{interactive}}{G_{locked}} \quad (3)$$

249 Based on the results shown in Fig. 4, we assume 1) the variances associated with the shortwave
 250 and longwave radiative flux in the locked-clouds run are very small (Figs. 4b,e), 2) the variances
 251 associated other terms in the surface energy budget in the locked-clouds runs are approximately
 252 equal to those in the interactive run (compare Figs. 4g,h; Figs. 4j,k; Figs. 4m,n) and 3) the percent-
 253 age contributions from the longwave radiative flux to the total variance can be neglected (Fig. 4f).

254 Based on the above, the first term in the RHS of Eq. 3 can be written as:

$$\frac{\sigma_{\Sigma \text{ interactive}}^2}{\sigma_{\Sigma \text{ locked}}^2} \approx \frac{\sigma_{\Sigma \text{ interactive}}^2}{(\sigma_{LH}^2 + \sigma_{SH}^2 + \sigma_{EK}^2 + \sigma_{geo}^2)_{\text{interactive}}} \approx \frac{1}{1 - (\frac{\sigma_{SW}^2}{\sigma_{\Sigma}^2})_{\text{interactive}}}. \quad (4)$$

255 The simple scaling in Eq. 4 suggests that 1) the changes in the total variance of the surface energy
256 flux between the interactive and locked-clouds simulations (LHS of Eq. 4) should peak over re-
257 gions where 2) the shortwave cloud flux variance makes the largest contribution to the total energy
258 flux variance in the interactive simulation (i.e., as shown in Fig. 4c).

259 Figure 5 quantifies the contributions of the various ratios in Eqs. 3–4 to the changes in temper-
260 ature variance between the interactive and locked simulations. Figure 5a reproduces the ratios of
261 the temperature variances from Fig. 1c (i.e., it shows the LHS of Eq. 3). Figure 5b shows the prod-
262 uct of the ratios between the interactive and locked simulations of 1) the surface flux and transport
263 variances, 2) the “efficiency” factors (e), and 3) “transfer” factors (G) (i.e., it shows the RHS of
264 Eq. 3). Figure 5c shows the first factor only from the RHS of Eq. 3, which is equivalent to the
265 sum of the results in the left column in Fig. 4 ($\sigma_{\Sigma \text{ interactive}}^2$) divided by the sum of the results in the
266 middle column ($\sigma_{\Sigma \text{ locked}}^2$). Figure 5d shows the results of the scaling approximation from Eq. 4,
267 which highlights the role of the shortwave radiative fluxes in the decomposition in Fig. 5c.

268 Comparing the results in Figs. 5a–c, it is clear that the ratios of SST variances between the in-
269 teractive and locked simulations (Fig. 5a) can be qualitatively reproduced by the decomposition
270 given in Eq. 3 (Fig. 5b). The decomposition, in turn, is dominated by the first factor on the RHS
271 of Eq. 3. That is, the increases in SST variance in the interactive simulation arise primarily from
272 the increases in the variance of the surface energy fluxes (Fig. 5c). The other two factors on the
273 RHS of Eq. 3 (i.e., the “efficiency” and “transfer” factors) are dominated by 1) decreases in the
274 covariances between the radiative fluxes in the locked run and 2) weak increases in SST persis-
275 tence in the tropical and extratropical oceans in the interactive run (Fig. C1). However, they play

276 a relatively small role in the amplification of tropical SST variance between the interactive and
277 locked simulations, as evidenced by the similarities between Figs. 5b and 5c. The fact that the dif-
278 ferences in SST variance between the interactive and locked simulations peak at tropical latitudes
279 (Fig. 5a) is consistent with the fact that the shortwave radiative fluxes play a more prominent role
280 in the total variance of the surface energy fluxes at tropical latitudes than they do at extratropical
281 latitudes (Figs. 4c and 5d; Eq. 4).

282 The key results in Figs. 4 and 5 are thus:

- 283 1) the preponderance of the differences in monthly-mean SST variance between the interactive
284 and locked simulations (Fig. 1c) arise from the attendant differences in the monthly-mean
285 shortwave radiative flux variances (Figs. 4a and 4b), and
- 286 2) the differences in monthly-mean SST variance peak in the tropics (Fig. 1c) since the variance
287 in the shortwave radiative fluxes accounts for a relatively large fraction of the total variances in
288 the surface energy budget there (Figs. 4c and 5d).

289 *b. Time series of interactive vs locked cloud fields*

290 Why does the variance of the monthly-mean shortwave radiative flux increase when clouds are
291 coupled to the atmospheric circulation? To understand this, we first consider the power spectrum
292 of two standardized, random time series: 1) a white noise time series and 2) a red-noise time
293 series with lag-one autocorrelation of $r_1 = 0.9$. For the purpose of comparison to the numerical
294 model output, the increment between time steps is defined as two-hours. By construction, both
295 time series have the same variance: one. However, the white noise time series has larger variance
296 than the red noise time series at periods shorter than ~ 28 hours (i.e., 14 time steps), whereas the
297 red noise time series has much larger variance than the white noise time series at all periods longer

than \sim 28 hours (Fig. 6a). The cutoff period at which a standardized red noise time series exhibits larger variance than a standardized white noise time series ranges from \sim 14 time steps (i.e., 28 hours in the case of data sampled every 2 hours) when $r_1 = 0.9$ to about \sim 5 time steps (i.e., 10 hours) when $r_1 = 0.1$ (see dashed lines in Fig. 6a).

Now consider the time series of total cloud fraction at a sample tropical grid point from the control interactive model simulations sampled at two-hourly intervals (corresponding to radiation call). In the interactive simulation, the cloud fraction has memory from one radiation call (every two hours) to the next of roughly $r_1 \approx 0.9$. However, in the locked simulation - by construction - the cloud fraction has no memory from two-hour period to the next ($r_1 = 0$). The total variance of the cloud fraction time series is identical in both the interactive and locked simulations. However, as is the case for the idealized white and red noise time series, the differences in the variance of cloud fraction between the two simulations are a function of frequency. The variance of cloud fraction in the interactive simulation is less than the variance of cloud fraction in the locked simulation at periods less than \sim 24 hours, but exceeds the variance of cloud fraction in the locked simulation at periods greater than \sim 1 day (Fig. 6b).

Hence, the increases in the variances of cloud fraction - and thus in the variances in shortwave CREs (Figs. 4a) and SSTs (Fig. 5) – in the interactive simulations arise from the reddening of the cloud field when it is coupled to the atmospheric circulation. *The basic effect of two-way coupling between clouds and the atmospheric circulation in the simulation is thus to increase the variance of CREs on timescales longer than a few days at the expense of shorter timescales.* As noted earlier, the increased variances in shortwave CREs have largest effect on the variance in SSTs at tropical latitudes, where the shortwave radiative fluxes account for a large fraction of the total variance in the surface energy fluxes. They have only a weak effect on the variances in SSTs at

321 extratropical latitudes, where the shortwave radiative fluxes play a small role in the total variance
322 in the surface energy fluxes.

323 **5. Concluding remarks**

324 It is been long established that CREs play a central role in determining Earth's mean climate. It
325 is becoming increasingly clear that they also play a key role in Earth's climate variability across
326 a range of timescales. In two recent studies, Rädel et al. (2016) and Middlemas et al. (2019)
327 argue that the inclusion of coupling between the atmospheric circulation and clouds projects onto
328 the variance of the El Niño/Southern Oscillation, primarily due to the projection of longwave
329 or shortwave CREs onto ENSO physics. Here we argue that coupling between the atmospheric
330 circulation and CREs leads to a much broader and more basic effect on the climate system: Cloud
331 circulation coupling leads to increases in the variance of SSTs on timescales from weeks to decades
332 that are apparent throughout the tropical oceans (Figs. 1c and 2) and appear to transcend the linear
333 response to simulated ENSO variability (see Appendix and Fig. B1).

334 We hypothesize that the increases in tropical SST variance in the interactive simulation arise
335 from the “reddening” of shortwave CREs when clouds are coupled to the circulation. Coupling
336 between the atmospheric circulation and clouds increases the memory in clouds on subdaily and
337 day-to-day timescales (e.g., the e-folding timescale of cloud fraction is \sim 1–2 days in sample time
338 series drawn from the interactive simulation; Fig. 6). The reddening of the cloud field due to the
339 memory inherent in the large-scale atmospheric circulation leads to a reduction in the variance
340 of cloud fraction on timescales less than a few days, but large increases in the variance of cloud
341 fraction on timescales greater than a few days (Fig. 6). Decomposition of the surface energy budget
342 (Figs. 4 and 5) reveals that it is the resulting increases in the variance of monthly-mean shortwave
343 CREs that lead to the increases in SST variance when clouds are coupled to the circulation. The

344 increases in SST variance are most clear in the tropics, where the shortwave heat fluxes account
345 for the largest fraction of the total variance in the surface energy budget (Figs. 4c and 5d). They
346 are less clear in the extratropics, where SST variability is dominated by the surface turbulent heat
347 fluxes (Fig. 4i).

348 The hypothesis accounts for enhanced SST variability on timescales spanning weeks to decades
349 throughout the tropical oceans when clouds are coupled to the atmospheric circulation. A key as-
350 sumption in the hypothesis is that cloud-circulation coupling does not change the total variance in
351 clouds and CREs (i.e., by construction the total variance is held fixed in the locked and interactive-
352 cloud simulations). Rather cloud-circulation coupling is theorized to impart memory to - and thus
353 enhance the low-frequency variance of - clouds and their radiative effects. Such memory would
354 not exist in the absence of the coupling of clouds to large-scale dynamics.

355 It is difficult to quantitatively compare our results with those published in Rädel et al. (2016)
356 and Middlemas et al. (2019) without reproducing their simulations in the climate model used here.
357 Hence, it is unclear whether the differences in results between our study and those studies arises
358 from differences in 1) the locking methodologies or 2) the cloud-radiative feedbacks and cloud-
359 circulation coupling schemes used in the different climate models. Additionally, we analyzed
360 output from the Rädel et al. (2016)'s experiment and found a large discontinuity in the changes in
361 variance in 1) surface temperature and 2) lower and upper tropospheric temperature between their
362 locked-cloud and interactive-cloud simulations. The discontinuity in surface and tropospheric
363 temperature variance changes renders it difficult to interpret the changes in SST variance in their
364 simulation (see Appendix D). It would be interesting to explore and test the robustness of our
365 hypothesis in climate models with different representations of CREs and in geographic regions
366 corresponding to different convective regimes (i.e., cloud-circulation coupling is a function of
367 convective regime; Bony and Dufresne 2005).

368 The results shown here reveal the remarkable effect that cloud-circulation coupling has on the
369 amplitude of SST variability on intraseasonal, interannual and even decadal time scales (Figs. 1c
370 and 2). Hence a key implication of our hypothesis is that the amplitude of SST variability in
371 numerical simulations depends critically on model renditions of CREs and cloud-circulation cou-
372 pling. This is important, since tropical SSTs provide a source of potential predictability for the
373 climate system across a range of timescales, and are linked to a host of surface climate impacts
374 throughout the tropics and extratropics. The implications of our hypothesis for climate impacts
375 and predictability are being explored for a companion study.

376 *Acknowledgment.* We thank Thorsten Mauritsen for assistance with the numerical model out-
377 put. We gratefully acknowledge three anonymous reviewers whose insightful comments led to
378 significant improvements to the manuscript. We also thank Eleanor A. Middlemas and Kevin
379 M. Grise for providing comments and suggestions. Y.L. is funded by NSF Climate and Large-
380 ScaleDynamics (AGS-1547003) and NASA JPL (1439268). D.W.J.T. is funded by NSF Climate
381 and Large-Scale Dynamics (AGS-1343080 and AGS-1547003). D.O. is funded by the Max Planck
382 Society (MPG). We thank the German Climate Computing Centre (DKRZ) for providing extensive
383 computational resources.

384

APPENDIX A

385

Decomposition of the factors that contribute to the variance in SST

386 The variance of SST is derived from the surface energy equation (Eq. 1), and follows Yu and Boer
387 (2006). Taking the centered difference of Eq. 1:

$$C_o \frac{T'(t + \Delta t) - T'(t - \Delta t)}{2\Delta t} = Q'_{SW} + Q'_{LW} + Q'_{LH} + Q'_{SH} + Q'_{EK} + Q'_{geo}, \quad (A1)$$

388 where Δt is 1 month.

³⁸⁹ Taking the square of Eq. A1 and the time average (denoted by overbar), the *lhs* of the resulting
³⁹⁰ equation is approximately equal to

$$\begin{aligned} &\approx \frac{C_o^2}{2(\Delta t)^2} \left(\overline{T(t)'^2} - \overline{T'(t + \Delta t)T'(t - \Delta t)} \right) \\ &= \frac{C_o^2(1 - r_2)}{2(\Delta t)^2} \sigma_T^2 \end{aligned} \quad (\text{A2})$$

³⁹¹ where σ_T^2 is the variance of the monthly-mean SST anomaly, and r_2 is lag-2 autocorrelation of
³⁹² SST anomaly computed as $\frac{\overline{T'(t + \Delta t)T'(t - \Delta t)}}{\overline{T(t)^2}}$.

³⁹³ The *rhs* of the square and time average of Eq. A1 is equal to:

$$\sigma_{\Sigma}^2 + 2\Sigma(\text{cov}(Q_i, Q_j)), \quad (\text{A3})$$

³⁹⁴ where σ_{Σ}^2 is the total variances of the six heat fluxes and transport related variances: $\sigma_{\Sigma}^2 = \sigma_{SW}^2 +$
³⁹⁵ $\sigma_{LW}^2 + \sigma_{LH}^2 + \sigma_{SH}^2 + \sigma_{EK}^2 + \sigma_{geo}^2$; and $\Sigma(\text{cov}(Q_i, Q_j))$ is the summed covariances of the individual
³⁹⁶ six components: $\Sigma(\text{cov}(Q'_i, Q'_j)) = \text{cov}(Q'_{SH}, Q'_{LH}) + \text{cov}(Q'_{SH}, Q'_{SW}) + \text{cov}(Q'_{SH}, Q'_{EK}) + \dots$. Note
³⁹⁷ that the variances and covariances terms involving the radiation fluxes are approximately zero in
³⁹⁸ the locked-clouds simulation (e.g., Figs. 4b, e).

³⁹⁹ Thus the variance of the SST can be approximately estimated from Eqs. A2–A3 as:

$$\sigma_T^2 = \frac{2(\Delta t)^2}{C_o^2(1 - r_2)} (\sigma_{\Sigma}^2 + 2\Sigma(\text{cov}(Q_i, Q_j))) \quad (\text{A4})$$

$$= G \cdot \sigma_{\Sigma}^2 \cdot e \quad (\text{A5})$$

⁴⁰⁰ where $G = \frac{2(\Delta t)^2}{C_o^2(1 - r_2)}$, $e = 1 + \frac{2\Sigma(\text{cov}(Q_i, Q_j))}{\sigma_{\Sigma}^2}$.

APPENDIX B

The robustness of the changes in SST variance to changes in ENSO variability

⁴⁰² Figures 1c and 2 reveal that coupled CREs leads to increases in SST variance not only in the
⁴⁰³ tropical central/eastern Pacific, but also in the tropical western Pacific, tropical Indian and Atlantic

405 oceans. Figure B1 tests whether the changes in SST variance outside the central/eastern tropical
406 Pacific can be explained as linear response to SST anomalies in the ENSO region. The figure is
407 identical to Figures 1, expect that the Ni no3.4 index has been linearly regressed from the SST data
408 at every grid point. The regression is based on contemporaneous values of the SST field and the
409 ENSO index, but similar results are derived after lagging the SST field by three months and with
410 other ENSO indices (not shown). By construction, the regression does not account for non-linear
411 relationships between ENSO variability and the SST field. As illustrated in Fig. B1, the increases
412 in SST variances outside the eastern tropical Pacific are not linearly related to changes in SST
413 variability in the ENSO region, and thus appear to occur independently of the model ENSO.

414

APPENDIX C

415

The contributions of “efficiency factor” e and “transfer factor” G

416 Figure 5c shows the first term on the *rhs* of Eq. 3 (i.e., the ratios of the surface flux and transport
417 variances). Here in Fig. C1 we show the contributions of the second and third terms in the *rhs* of
418 Eq. 3. Panel (a) shows the ratios of the “efficiency factors” - which arise mainly from differences
419 in the sum of the covariances between the heat flux terms. Panel (b) shows the ratios of the
420 “transfer factors”- which arise from differences in SST persistence as calculated from the lag-2
421 auto-correlation. The ratios in the “efficiency factors” are generally less than 1, indicating the
422 covariance terms are generally smaller in the interactive-cloud simulation than they are in the
423 locked-cloud simulation. The ratios of the “transfer factors” are generally positive since SST
424 persistence is slightly longer in the interactive simulation. Overall, the changes in the two factors
425 are relatively weak relative to the changes in the variances of the surface energy fluxes (Fig. 5c).

426

APPENDIX D

Comparison with Rädel et al. (2016)

428 The results in our study and those in Rädel et al. (2016) offer very different interpretations of the
 429 role of CRE on tropical SSTs. We argue that cloud/circulation coupling leads to enhanced variance
 430 of SSTs across the tropics due to the enhance persistence of SW CREs. Radel et al. (2016) argue
 431 that cloud/circulation coupling leads to enhanced variance of SSTs in the eastern tropical Pacific
 432 due to the projection of LW CREs onto ENSO physics.

433 We also examined the numerical output used in the Rädel et al. (2016) study. In doing so, we
 434 uncovered a discontinuity in the temperature variance changes between their interactive-clouds
 435 and locked-clouds simulations. The discontinuity renders it difficult to compare their results to
 436 ours.

437 As an example, the left column in Figure D1 shows the standard deviation in surface temperature
 438 and 2m temperature from their interactive-clouds simulation. The right column shows the standard
 439 deviation of the same fields from the locked-clouds simulation (as reviewed in the Introduction of
 440 this study). As noted in Rädel et al. (2016), the variance of surface temperature is slightly weaker
 441 in the eastern tropical Pacific when clouds are locked (compare panels a and b). However, the
 442 decreases in surface temperature variance in the Pacific are overwhelmed by very large increases
 443 in 2m temperature variance (by factors of $\sim 3\text{--}5$) that occur across much of the globe – especially
 444 over land areas – when clouds are locked (compare the changes between panels c and d with
 445 those between panels a and b). The variance increases in the locked-clouds run extend to the free
 446 tropospheric circulation (compare panels e and f).

References

448 Alexander, M. A., 1992: Midlatitude atmosphere-ocean interaction during El Niño. Part I: The
 449 North Pacific Ocean. *J. Climate*, **5**, 944–958.

- 450 Alexander, M. A., I. Bladé, M. Newman, J. R. Lanzante, N.-C. Lau, and J. D. Scott, 2002: The
451 atmospheric bridge: Influence of ENSO teleconnections on air-sea interaction over the global
452 oceans. *J. Climate*, **15**, 2205–2231.
- 453 Barsugli, J. J., and D. S. Battisti, 1998: The basic effects of atmosphereocean thermal coupling on
454 midlatitude variability. *J. Atmos. Sci.*, **55**, 477–493.
- 455 Bellenger, H., E. Guilyardi, J. Leloup, M. Lengaigne, and J. Vialard, 2014: ENSO repre-
456 sentation in climate models: from CMIP3 to CMIP5. *Clim. Dynam.*, **42**, 1999–2018, doi:
457 10.1007/s00382-013-1783-z.
- 458 Bony, S., and J.-L. Dufresne, 2005: Marine boundary layer clouds at the heart of tropi-
459 cal cloud feedback uncertainties in climate models. *Geophys. Res. Lett.*, **33**, L17810, doi:
460 10.1029/2005GL023851.
- 461 Cayan, D. R., 1992: Latent and sensible heat flux anomalies over the northern oceans: driving the
462 sea temperature. *J. Phys. Oceanogr.*, **22**, 859–881.
- 463 Ceppi, P., and D. L. Hartmann, 2015: Connections between clouds, radiation, and midlatitude
464 dynamics: a review. *Curr. Clim. Change Rep.*, doi:10.1007/s4061-015-0010-x.
- 465 Ceppi, P., and D. L. Hartmann, 2016: Clouds and the atmospheric circulation response to warming.
466 *J. Climate*, **29**, 783–799, doi:10.1002/2014GL060043.
- 467 Ceppi, P., Y.-T. Hwang, D. M. W. Frierson, and D. L. Hartmann, 2012: Southern Hemisphere jet
468 latitude biases in CMIP5 models linked to shortwave cloud forcing. *Geophys. Res. Lett.*, **39**,
469 L19708, doi:10.1029/2012GL053115.

- 470 Ceppi, P., M. D. Zelinka, and D. L. Hartmann, 2014: The response of the Southern Hemispheric
471 eddy-driven jet to future changes in shortwave radiation in CMIP5. *Geophys. Res. Lett.*, **41**,
472 3244–3250, doi:10.1002/2014GL060043.
- 473 Chang, P., and Coauthors, 2006: Climate fluctuations of tropical coupled systems: the role of
474 ocean dynamic. *J. Climate*, **19**, 51225174.
- 475 Chen, Y., and A. D. D. Genio, 2009: Evaluation of tropical cloud regimes in observations and a
476 general circulation mode. *Clim. Dynam.*, **32**, 355–369, doi:10.1007/S00382-008-0386-6.
- 477 Crueger, T., and B. Stevens, 2015: The effect of atmospheric radiative heating by clouds on the
478 Madden-Julian Oscillation. *J. Adv. Model. Earth Syst*, doi:10.1002/2015MS000434.
- 479 Davis, R. E., 1976: Predictability of sea surface temperature and sea level pressure anomalies over
480 the North Pacific Ocean. *J. Phys. Oceanogr.*, **6**, 249–266.
- 481 Eguchi, N., and M. Shiotani, 2004: Intraseasonal variations of water vapor and cirrus clouds in the
482 tropical upper troposphere. *J. Geophys. Res.*, **109**, D12 106, doi:10.1029/2003JD004314.
- 483 Eyring, V., S. Bony, G. A. Meehl, C. A. Senior, B. Stevens, R. J. Stouffer, and K. E. Taylor, 2016:
484 Overview of the Coupled Model Intercomparison Project Phase 6 (CMIP6). *Geosci. Model Dev.*,
485 **9**, 1937–1958, doi:10.5194/gmd-9-1937-2016.
- 486 Fermepin, S., and S. Bony, 2014: Influence of low-cloud radiative effects on tropical circulation
487 and precipitation. *J. Adv. Model. Earth Syst*, **06**, doi:10.1002/2013MS000288.
- 488 Fläschner, D., T. Mauritsen, B. Stevens, and S. Bony, 2018: The signature of shallow circulations,
489 not cloud radiative effects, in the spatial distribution of tropical precipitation. *J. Climate*, 9489–
490 9505, doi:10.1175/JCLI-D-18-0230.1.

- 491 Harrop, B. E., and D. L. Hartmann, 2016: The role of cloud radiative heating in determining
492 the location of the ITCZ in aquaplanet simulations. *J. Climate*, **29**, 2741–2763, doi:10.1175/
493 JCLI-D-15-0521.1.
- 494 Hartmann, D. L., 1994: *Global Physical Climatology*. Academic Press, San Diego, CO, USA, 411
495 pp.
- 496 Jiang, X., D. E. Waliser, J.-L. Li, and C. Woods, 2011: Vertical structures of cloud water associated
497 with the boreal summer intraseasonal oscillation based on CloudSat observations and ERA-
498 Interim reanalysis. *Clim. Dynam.*, **10**, doi:10.1007/s00382-010-0853-8.
- 499 Langen, P. L., R. G. Graversen, and T. Mauritsen, 2012: Separation of contributions from radiative
500 feedbacks to polar amplification on an aquaplanet. *J. Climate*, **25**, 3010–3024, doi:10.1175/
501 JCLI-D-11-00246.1.
- 502 Lee, M.-I., I.-S. Kang, J.-K. Kim, and B. E. Mapes, 2001: Influence of cloud-radiation interaction
503 on simulating tropical intraseasonal oscillation with an atmospheric general circulation model.
504 *J. Geophys. Res.*, **106**, 14 219–14 233, doi:10.1029/2001JD900143.
- 505 Li, Y., and D. W. J. Thompson, 2016: Observed signatures of the barotropic and baroclinic annular
506 modes in cloud vertical structure and cloud radiative effects. *J. Climate*, **29**, 4723–4740.
- 507 Li, Y., D. W. J. Thompson, and S. Bony, 2015: The influence of atmospheric cloud ra-
508 diative effects on the large-scale atmospheric circulation. *J. Climate*, **28**, 7263–7278, doi:
509 10.1175/JCLI-D-14-00825.1.
- 510 Li, Y., D. W. J. Thompson, S. Bony, and T. M. Merlis, 2019: Thermodynamic control on the
511 poleward shift of the extratropical jet in climate change simulations. *J. Climate*, **32**, 917–934.

- 512 Li, Y., D. W. J. Thompson, and Y. Huang, 2017: The influence of atmospheric cloud radiative
513 effects on the large-scale stratospheric circulation. *J. Climate*, **30**, 5621–5635, doi:10.1175/
514 JCLI-D-16-0643.1.
- 515 Li, Y., D. W. J. Thompson, Y. Huang, and M. Zhang, 2014a: Observed linkages between the
516 Northern Annular Mode/North Atlantic Oscillation, cloud incidence, and cloud radiative forc-
517 ing. *Geophys. Res. Lett.*, **41**, 1681–1688, doi:10.1002/2013GL059113.
- 518 Li, Y., D. W. J. Thompson, G. L. Stephens, and S. Bony, 2014b: A global survey of the linkages
519 between cloud vertical structure and large-scale climate. *J. Geophys. Res.*, **119**, 3770–3792,
520 doi:10.1002/2013JD020669.
- 521 Lin, J.-L., D. Kim, M. Lee, and I. Kang, 2007: Effects of cloudradiative heating on atmospheric
522 general circulation model (AGCM) simulations of convectively coupled equatorial waves. *J.*
523 *Geophys. Res.*, **112**, D24 107, doi:10.1029/2006JD008291.
- 524 Lloyd, J., E. Guilyardi, and H. Weller, 2011: The role of atmosphere feedbacks during ENSO in
525 the CMIP3 models. Part II: using AMIP runs to understand the heat flux feedback mechanisms.
526 *Clim. Dynam.*, **37**, 1271–1292, doi:10.1007/s00382-010-0895-y.
- 527 Lloyd, J., E. Guilyardi, and H. Weller, 2012: The role of atmosphere feedbacks during ENSO
528 in the CMIP3 Models. Part III: The shortwave flux feedback. *J. Climate*, **25**, 4275–4293, doi:
529 10.1175/JCLI-D-11-00178.1.
- 530 Ma, D., and Z. Kuang, 2011: Modulation of radiative heating by the Madden-Julian Oscilla-
531 tion and convectively coupled Kelvin Waves as observed by CloudSat. *Geophys. Res. Lett.*, **38**,
532 L21 813.

- 533 Marshall, J., H. Johnson, and J. Goodman, 2001: A study of the interaction of the North Atlantic
534 Oscillation with ocean circulation. *J. Climate*, **14**, 1399–1421.
- 535 Masunaga, H., M. Satoh, and H. Miura, 2008: A joint satellite and global cloud-resolving
536 model analysis of a Madden-Julian Oscillation event: Model diagnosis. *J. Geophys. Res.*, **113**,
537 D17210, doi:10.1029/2008JD009986.
- 538 Mauritsen, T., R. G. Graversen, D. Klocke, P. L. Langen, B. Stevens, and L. Tomassini,
539 2013: Climate feedback efficiency and synergy. *Clim. Dynam.*, **41**, 2539–2554, doi:10.1007/
540 s00382-013-1808-7.
- 541 Mauritsen, T., and Coauthors, 2012: Tuning the climate of a global model. *J. Adv. Model. Earth
542 Syst.*, **4**, M00A01, doi:10.1029/2012MS000154.
- 543 Middlemas, E. A., A. C. Clement, B. Medeiros, and B. Kirtman, 2019: Cloud radiative feedbacks
544 and El Niño Southern Oscillation. *J. Climate*, **32**, 4661–4680, doi:10.1175/jcli-d-18-0842.1.
- 545 Miller, A. J., 1992: Large-scale ocean-atmosphere interactions in a simplified coupled model of
546 the midlatitude wintertime circulation. *J. Atmos. Sci.*, **49**, 273–286.
- 547 Olonscheck, D., T. Mauritsen, and D. Notz, 2019: Arctic sea-ice variability is primarily
548 driven by atmospheric temperature fluctuations. *Nature Geosci.*, **12**, 430434, doi:10.1038/
549 s41561-019-0363-1.
- 550 Rädel, G., T. Mauritsen, B. Stevens, D. Dommegård, D. Dommegård, D. Matei, K. Bellomo,
551 and A. Clement, 2016: Amplification of El Niño by cloud longwave coupling to atmospheric
552 circulation. *Nature Geoscience*. *Nature Geosci.*, **9**, 106–110.

- 553 Riley, E. M., B. E. Mapes, and S. N. Tulich, 2011: Clouds Associated with the Madden Julian
554 Oscillation: A New Perspective from CloudSat. *J. Atmos. Sci.*, **68**, 3032–3051, doi:10.1175/
555 JAS-D-11-030.1.
- 556 Schneider, E. K., B. P. Kirtman, and R. S. Lindzen, 1999: Tropospheric water vapor and climate
557 sensitivity. *J. Atmos. Sci.*, **56**, 1649–1658.
- 558 Schott, F. A., S.-P. Xie, and J. P. McCreary, 2009: Indian Ocean circulation and climate variability.
559 *Rev. Geophys.*, **47**, RG1002, doi:10.1029/2007RG000245.
- 560 Stephens, G., and Coauthors, 2002: The CloudSat mission and the A-train: A new dimension of
561 space-based observations of clouds and precipitation. *Bull. Amer. Meteor. Soc.*, **83**, 1771–1790,
562 doi:10.1175/BAMS-83-12-1771.
- 563 Su, H., and J. H. Jiang, 2013: Tropical clouds and circulation changes during the 2006-07 and
564 2009-10 El Niños. *J. Climate*, **26**, 399–413, doi:10.1175/JCLI-D-12-00152.1.
- 565 Su, H., J. H. Jiang, J. Teixeira, A. Gettelman, X. Huang, G. Stephens, D. Vane, and V. S. Perun,
566 2011: Comparison of regime-sorted tropical cloud profiles observed by CloudSat with GEOS5
567 analyses and two general circulation model simulations. *J. Geophys. Res.*, **116**, D09104, doi:
568 10.1029/2010JD014971.
- 569 Tromer, E., and W. B. Rossow, 2010: Interaction of tropical deep convection with the large-scale
570 circulation in the MJO. *J. Climate*, **23**, 1837–1853, doi:10.1175/2009JCLI3240.1.
- 571 Voigt, A., N. Albern, and G. Papavasileiou, 2019: The atmospheric pathway of the cloud-radiative
572 impact on the circulation response to global warming: Important and uncertain. *J. Climate*, **32**,
573 3051–3067, doi:10.1175/JCLI-D-18-0810.1.

- 574 Voigt, A., and T. A. Shaw, 2015: Radiative changes of clouds and water vapor shape circulation
575 response to global warming. *Nature Geosci.*, **8**, 102106, doi:10.1038/ngeo2345.
- 576 Voigt, A., and T. A. Shaw, 2016: Impact of regional atmospheric cloud radiative changes on shifts
577 of the extratropical jet stream in response to global warming. *J. Climate*, **29**, 8399–8421, doi:
578 10.1175/JCLI-D-16-0140.1.
- 579 Wall, C. J., and D. L. Hartmann, 2015: On the influence of poleward jet shift on Shortwave cloud
580 feedback in GCMs. *J. Adv. Model. Earth Syst.*, **07**, doi:10.1002/2015MS000520.
- 581 Watt-Meyer, O., and D. M. W. Frierson, 2017: Local and emote impacts of atmospheric cloud
582 radiative effects onto the eddy-driven jet. *Geophys. Res. Lett.*, **44**, 10 036–10 044, doi:10.1002/
583 2017GL074901.
- 584 Xie, S.-P., and J. A. Carton, 2004: Tropical atlantic variability: patterns, mechanisms, and impacts.
585 *Earth Climate: The Ocean-Atmosphere Interaction*, C. Wang, S.-P. Xie, and J. A. Carton, Eds.,
586 Am. Geophys. Union, Washington DC, 121–142.
- 587 Yu, B., and G. J. Boer, 2006: The variance of sea surface temperature and projected changes with
588 global warming. *Clim. Dynam.*, **26**, 801–821, doi:10.1007/s00382-006-0117-9.
- 589 Yuan, J., and R. A. Houze, 2013: Deep convective systems observed by A-Train in the trop-
590 ical Indo-Pacific region affected by the MJO. *J. Atmos. Sci.*, **70**, 456–486, doi:10.1175/
591 JAS-D-12-057.1.
- 592 Zhang, Y., S. Klein, G. G. Mace, and J. Boyl, 2007: Cluster analysis of tropical clouds using
593 CloudSat data. *Geophys. Res. Lett.*, **34**, L12 813, doi:10.1029/2007GL029336.
- 594 Zurovac-Jevtić, D., S. Bony, and K. Emanuel, 2006: On the role of clouds and moisture in tropical
595 waves: A two-dimensional model study. *J. Atmos. Sci.*, **63**, 2140–2154.

596 LIST OF FIGURES

- Fig. 1.** The effect of interactive clouds on SST variance. (a) Variances of monthly-mean SST anomalies from the 200-yr interactive-clouds run. (b) Variances of monthly-mean SST anomalies from the 200-yr locked-clouds run. (c) Ratio of the variances between the interactive and locked runs. Ratios >1 indicate larger variability in the interactive run, and vice versa. Stippling indicates regions where the ratios are significant at the 95% level. The black boxes in (c) are the regions used for calculating the power spectra of the area averaged SST anomalies in Fig. 2.

Fig. 2. Power spectra of SST anomaly time series for indicated regions. Power spectra of SST anomaly time series averaged over (a) Niño 3.4, (b) entire tropics (15°S – 15°N), (c) tropical Indian ocean (10°S – 10°N , 50° – 100°E), (d) tropical western Pacific (10°S – 10°N , 100°E – 180°), (e) tropical north Atlantic (0° – 15°N , 315° – 340°E), and (f) tropical south Atlantic (15°S – 0° , 20°W – 10°E). Results for the interactive-clouds simulation are indicated by the blue lines, and for the locked-clouds simulation are indicated by the red lines. Regions are indicated by the black boxes in Fig. 1c.

Fig. 3. The effects of interactive clouds on tropical climate. Ratio of the variances between the interactive and locked runs of (a) atmospheric temperature at 300 hPa, (b) convective precipitation, (c) geopotential height at 150 hPa, and (d) eddy geopotential height at 150 hPa. The black contours superimposed on panel d denote the long-term mean geopotential height at 150 hPa (contour interval: 14000, 14100, 14110, 14120, 14130 m...). Results in shading are based on monthly-mean anomalies.

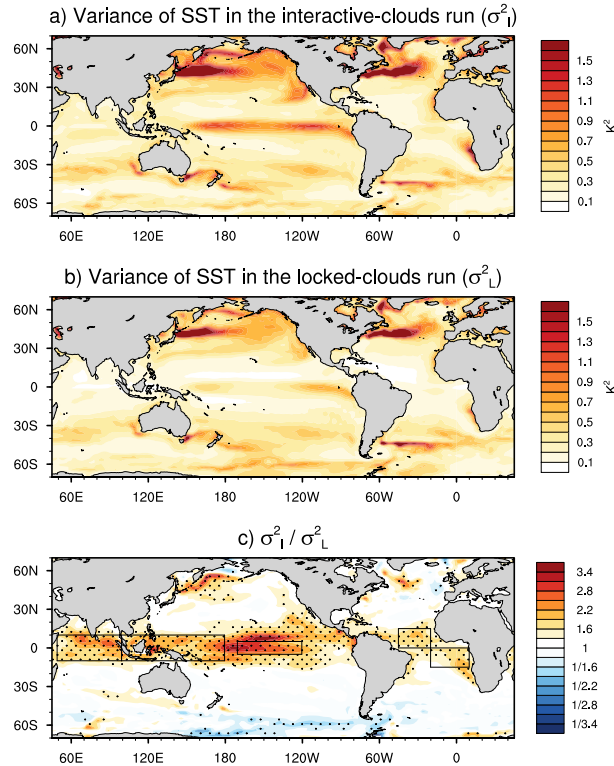
Fig. 4. Variances in the surface energy fluxes. (a, b) surface shortwave radiative flux, (d, e) long-wave radiative flux, (g, h) latent heat flux, (j, k) sensible heat flux, (m, n) heat advection by the meridional Ekman and geostrophic current. Results for (left column) the 200-yr interactive-clouds simulation and (middle column) the 200-yr locked-clouds simulation. The right column is the percentage contribution of each term to the total variance in the interactive-clouds simulation. Results are based on monthly-mean anomalies. The surface radiative flux are based on all-sky radiative flux, the variance in clear-sky radiative flux are of similar amplitude between the control and locked simulations.

Fig. 5. Identifying the physical factors responsible for the increases in SST variance. (a) The ratios of the surface temperature variance between the interactive and locked simulations (reproduced from Fig. 1c). (b) The product of all three terms on the *rhs* of Eq. 3. (c) The contribution of the ratios in the sums of the surface fluxes (the first factor on the *rhs* of Eq. 3). (d) The results of the approximation in Eq. 4, which highlights the dominant role of the SW radiative fluxes in the ratios shown in panel c (see text for details). Results are based on monthly-mean anomalies.

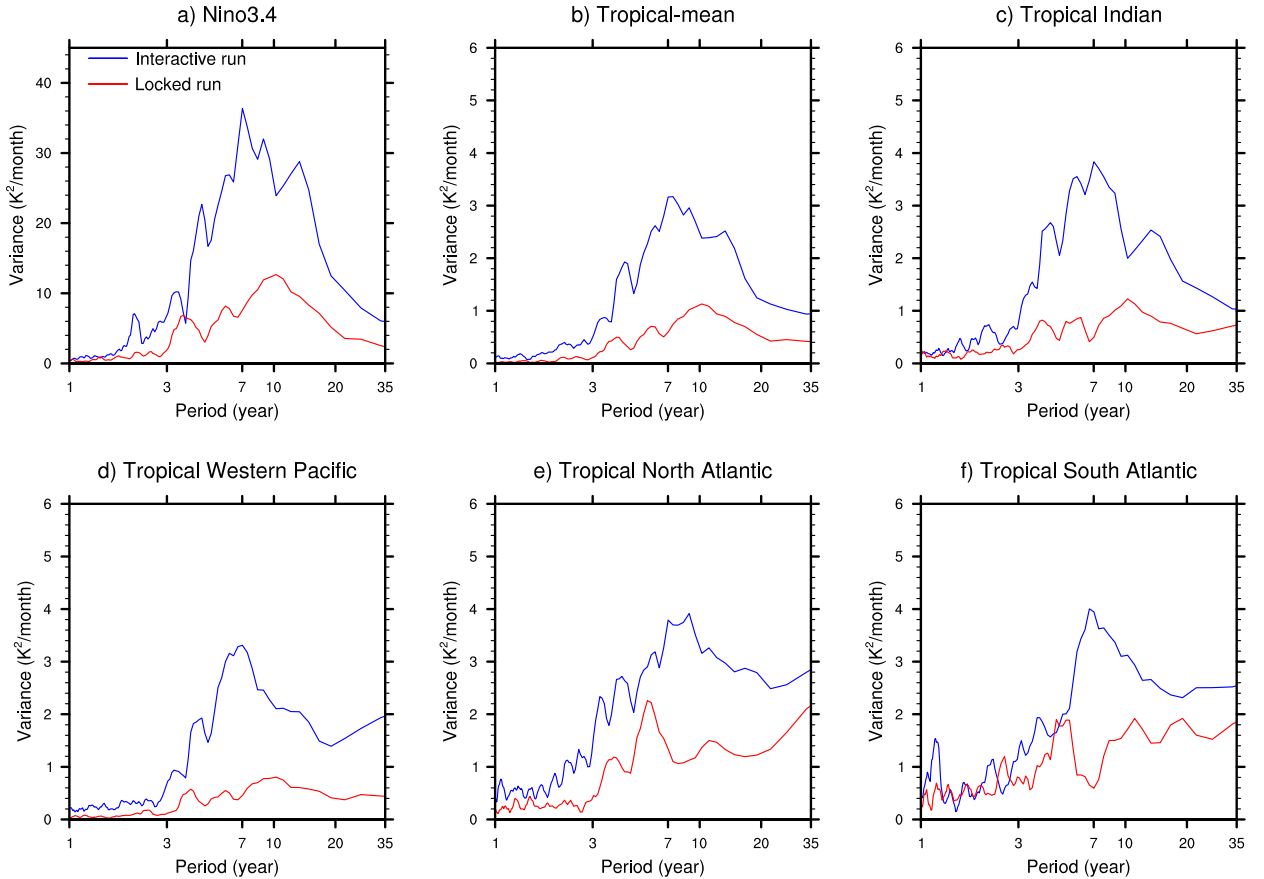
Fig. 6. The importance of persistence in the variance of cloud fraction. (a) Power spectra for a randomly generated red noise time series with lag-one autocorrelation of $r_1 = 0.9, 0.5$, and 0.1 (dashed lines) and a white noise time series with $r_1 = 0$ (solid line). (b) Power spectra for time series of cloud fraction at a sample tropical grid point ($0^{\circ}, 180^{\circ}$) used in the interactive-clouds run (dashed line) and the locked-clouds run (solid). The cloud fraction time series are 50-yr long and sampled at two-hourly intervals. The randomly generated time series used to construct the top panel are the same length and same time step interval as the cloud fraction time series.

Fig. B1. SST variances in the interactive and locked simulation after linearly removing the effects of ENSO from the data. Same as Fig. 1, but for results after subtracting linearly regressing the

642	Niño 3.4 index (SSTs averaged over 5°N–5°S, 170°W–120°W as indicated by black box in	37
643	panel c) from the SST data at all grid points.	
644	Fig. C1. As in Fig. 5c, but for (a) the ratios of the “efficiency” factors (the second term on the <i>rhs</i> of	
645	Eq. 3), and (b) the ratio of the “transfer” factors (the third term on the <i>rhs</i> of Eq. 3).	38
646	Fig. D1. Standard deviation of monthly-mean (top) surface temperature anomalies, (middle) temper-	
647	ature anomalies at 2m, and (bottom) temperature anomalies at 300 hPa from the 200-yr	
648	(left) interactive-clouds run and (right) locked-clouds run. Results are based on Rädel et al.	
649	(2016)’s output provided courtesy of Thorsten Mauritsen).	39



650 FIG. 1. The effect of interactive clouds on SST variance. (a) Variances of monthly-mean SST anomalies from
 651 the 200-yr interactive-clouds run. (b) Variances of monthly-mean SST anomalies from the 200-yr locked-clouds
 652 run. (c) Ratio of the variances between the interactive and locked runs. Ratios >1 indicate larger variability in
 653 the interactive run, and vice versa. Stippling indicates regions where the ratios are significant at the 95% level.
 654 The black boxes in (c) are the regions used for calculating the power spectra of the area averaged SST anomalies
 655 in Fig. 2.



656 FIG. 2. Power spectra of SST anomaly time series for indicated regions. Power spectra of SST anomaly
 657 time series averaged over (a) Niño 3.4, (b) entire tropics (15°S – 15°N), (c) tropical Indian ocean (10°S – 10°N ,
 658 50° – 100°E), (d) tropical western Pacific (10°S – 10°N , 100°E – 180°), (e) tropical north Atlantic (0° – 15°N , 315° –
 659 340°E), and (f) tropical south Atlantic (15°S – 0° , 20°W – 10°E). Results for the interactive-clouds simulation are
 660 indicated by the blue lines, and for the locked-clouds simulation are indicated by the red lines. Regions are
 661 indicated by the black boxes in Fig. 1c.

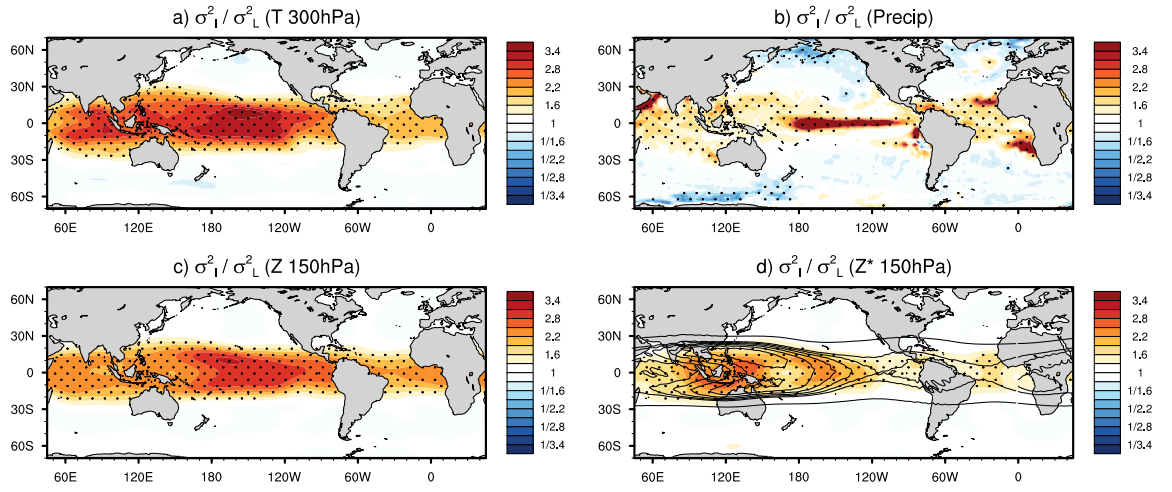


FIG. 3. The effects of interactive clouds on tropical climate. Ratio of the variances between the interactive and locked runs of (a) atmospheric temperature at 300 hPa, (b) convective precipitation, (c) geopotential height at 150 hPa, and (d) eddy geopotential height at 150 hPa. The black contours superimposed on panel d denote the long-term mean geopotential height at 150 hPa (contour interval: 14000, 14100, 14110, 14120, 14130 m...). Results in shading are based on monthly-mean anomalies.

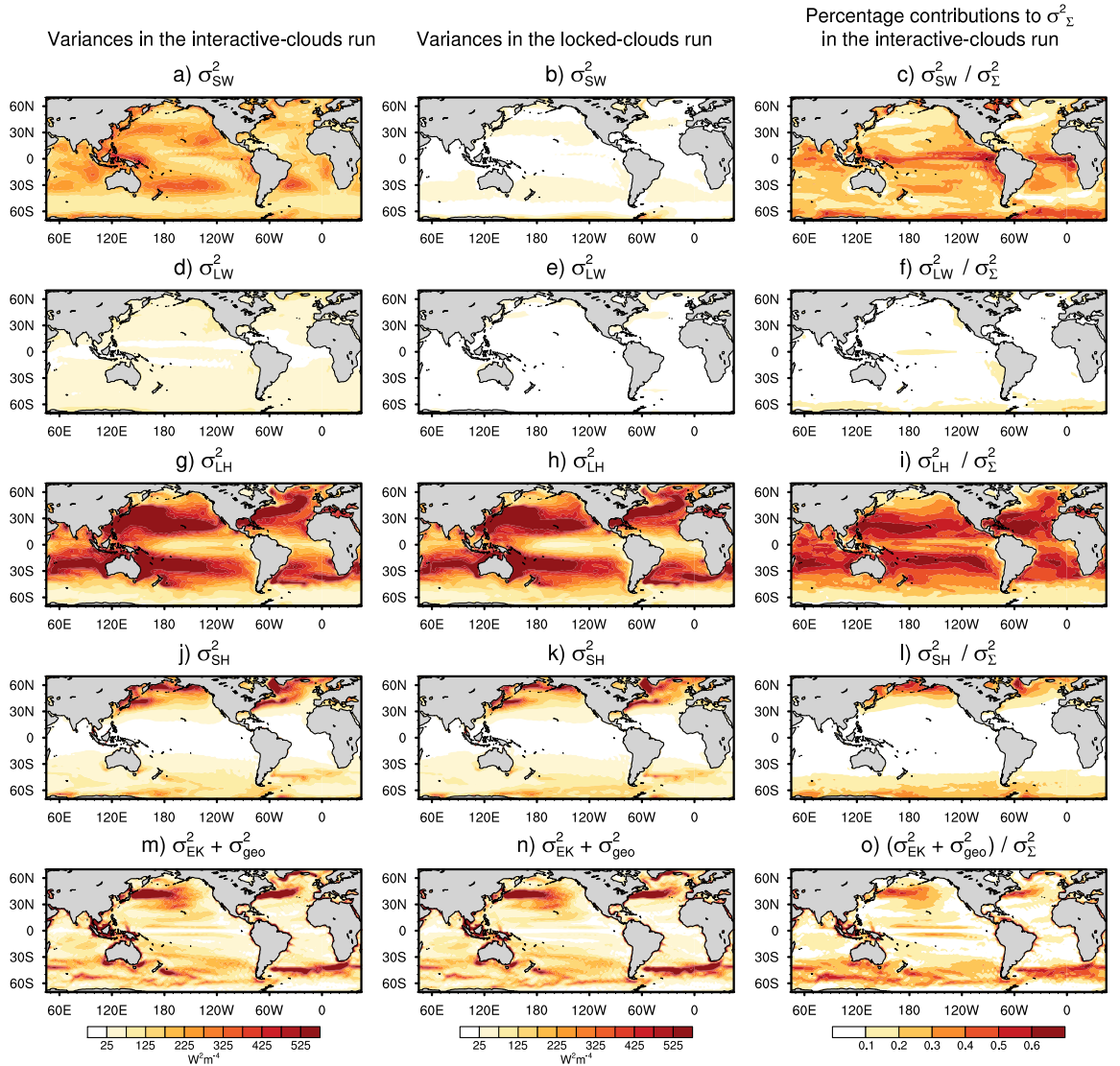
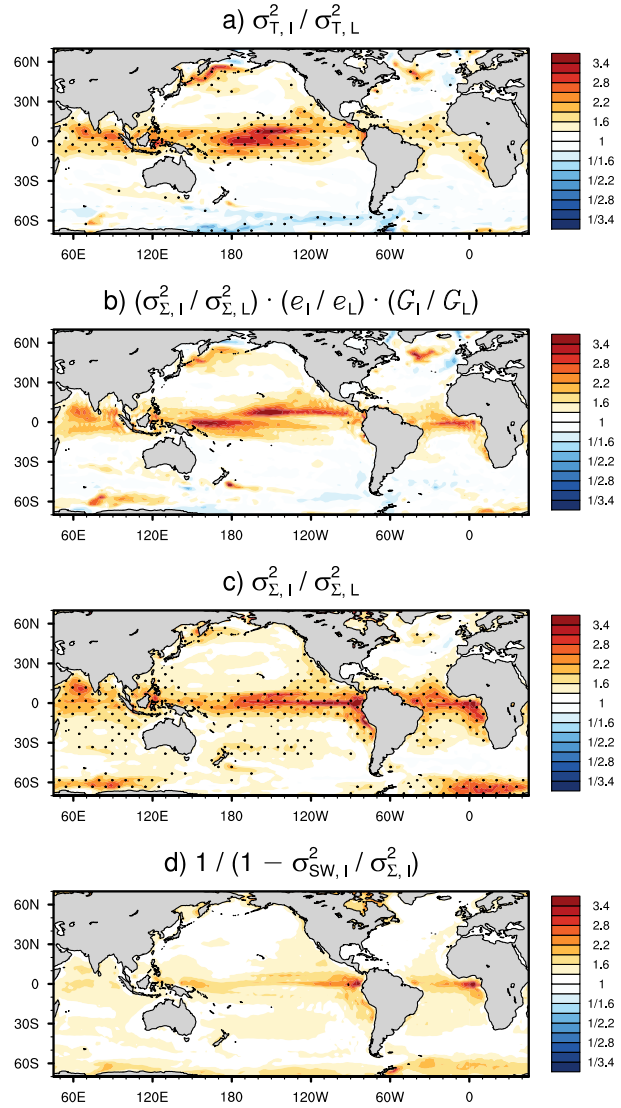
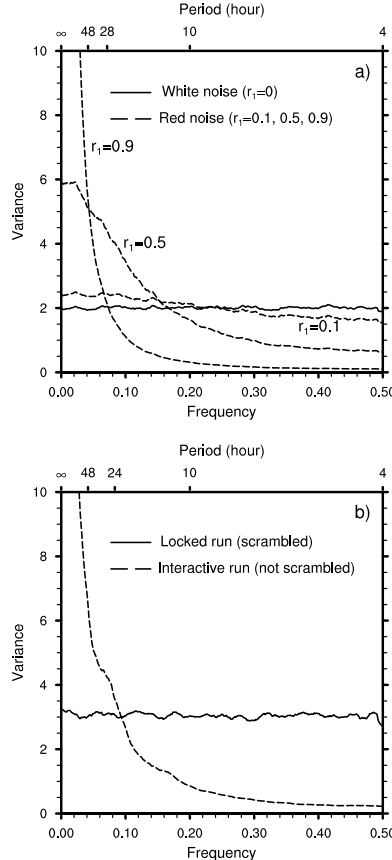


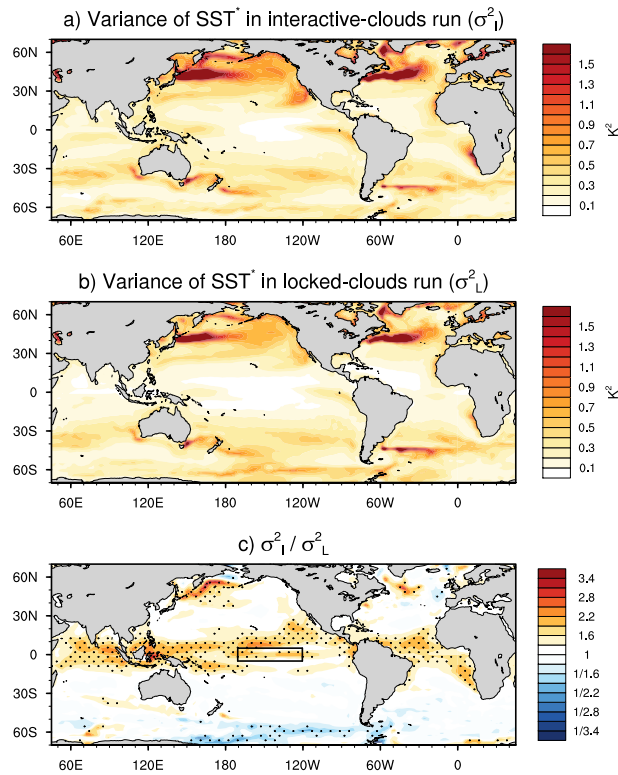
FIG. 4. Variances in the surface energy fluxes. (a, b) surface shortwave radiative flux, (d, e) longwave radiative flux, (g, h) latent heat flux, (j, k) sensible heat flux, (m, n) heat advection by the meridional Ekman and geostrophic current. Results for (left column) the 200-yr interactive-clouds simulation and (middle column) the 200-yr locked-clouds simulation. The right column is the percentage contribution of each term to the total variance in the interactive-clouds simulation. Results are based on monthly-mean anomalies. The surface radiative flux are based on all-sky radiative flux, the variance in clear-sky radiative flux are of similar amplitude between the control and locked simulations.



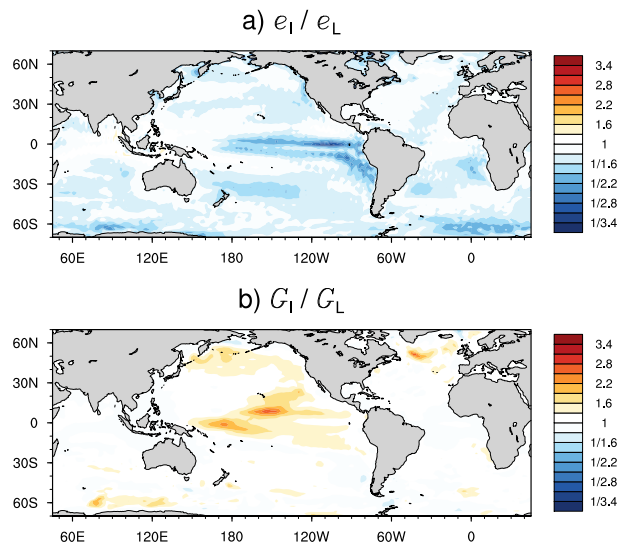
674 FIG. 5. Identifying the physical factors responsible for the increases in SST variance. (a) The ratios of the
 675 surface temperature variance between the interactive and locked simulations (reproduced from Fig. 1c). (b) The
 676 product of all three terms on the *rhs* of Eq. 3. (c) The contribution of the ratios in the sums of the surface
 677 fluxes (the first factor on the *rhs* of Eq. 3). (d) The results of the approximation in Eq. 4, which highlights the
 678 dominant role of the SW radiative fluxes in the ratios shown in panel c (see text for details). Results are based
 679 on monthly-mean anomalies.



680 FIG. 6. The importance of persistence in the variance of cloud fraction. (a) Power spectra for a randomly
 681 generated red noise time series with lag-one autocorrelation of $r_1 = 0.9, 0.5$, and 0.1 (dashed lines) and a white
 682 noise time series with $r_1 = 0$ (solid line). (b) Power spectra for time series of cloud fraction at a sample tropical
 683 grid point ($0^\circ, 180^\circ$) used in the interactive-clouds run (dashed line) and the locked-clouds run (solid). The cloud
 684 fraction time series are 50-yr long and sampled at two-hourly intervals. The randomly generated time series used
 685 to construct the top panel are the same length and same time step interval as the cloud fraction time series.

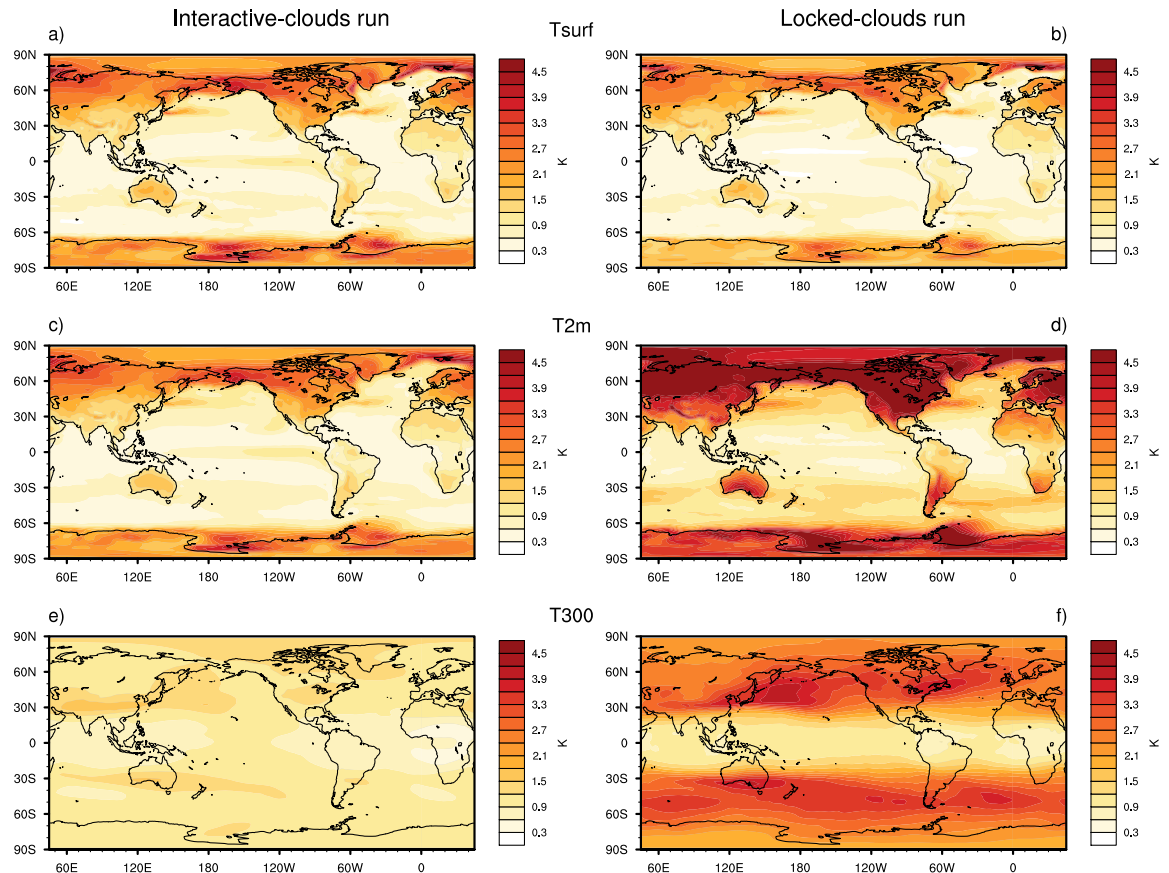


686 Fig. B1. SST variances in the interactive and locked simulation after linearly removing the effects of ENSO
 687 from the data. Same as Fig. 1, but for results after subtracting linearly regressing the Niño 3.4 index (SSTs
 688 averaged over 5°N – 5°S , 170°W – 120°W as indicated by black box in panel c) from the SST data at all grid
 689 points.



690 Fig. C1. As in Fig. 5c, but for (a) the ratios of the “efficiency” factors (the second term on the *rhs* of Eq. 3),
 691 and (b) the ratio of the “transfer” factors (the third term on the *rhs* of Eq. 3).

Radel et al. (2016) Output



692 Fig. D1. Standard deviation of monthly-mean (top) surface temperature anomalies, (middle) temperature
 693 anomalies at 2m, and (bottom) temperature anomalies at 300 hPa from the 200-yr (left) interactive-clouds run
 694 and (right) locked-clouds run. Results are based on Rädel et al. (2016)'s output provided courtesy of Thorsten
 695 Mauritzen).